A novel laboratory apparatus for simulating isotropic oceanic turbulence at low Reynolds number

Donald R. Webster[1], Aisha Brathwaite[1], and Jeannette Yen[2]
[1]School of Civil & Environmental Engineering, Georgia Institute of Technology, Atlanta, GA, USA 30332
[2]School of Biology, Georgia Institute of Technology, Atlanta, GA, USA 30332

Abstract

A new experimental apparatus to simulate oceanic turbulence at low Reynolds number in the laboratory is described. Actuators located at each corner of a cubic Plexiglas box generated synthetic jets that interacted to create turbulent flow at the center of the saltwater apparatus. Four turbulent intensity levels were established, and velocity measurements were performed using digital particle image velocimetry. The flow characteristics in the center of the apparatus were confirmed to be nearly isotropic and homogeneous. The range of the dissipation rate (10^{-3} to 1 cm²s⁻³) and the Kolmogorov microscale (0.03 to 0.2 cm) agreed well with natural oceanic environments in the coastal zone, and the length scales and magnitude of the velocity and strain rate fluctuations were appropriate for zooplankton studies. The flow characteristics compared favorably with previous approaches for generating turbulence in the laboratory, in particular, oscillating-grid apparatus. The current design also possessed increased simplicity, controllability, and transportability. Future objectives include studying the behavioral response of zooplankton to turbulent fluid motions.

Small organisms in the ocean, such as zooplankton, are subject to fluid forces imposed by the turbulent velocity field. For instance, turbulent motion increases the contact rate among organisms (Rothschild and Osborn 1988; Saiz and Kiørboe 1995; Dower et al. 1997, 1998; MacKenzie and Kiørboe 2000) and also appears to induce a behavior response (Incze et al. 2001; Franks 2001). Studies indicate that several plankton species may avoid active turbulent surface layers by swimming downward to the pycnocline (Heath et al. 1988; Mackas et al. 1993; Lagadeuc et al. 1997; Incze et al. 2001). These observations suggest that the vertical variation of turbulence exerts an influence on vertical migratory behavior (Franks 2001; Incze et al. 2001). Other observations suggest that horizontal distributions can be influenced by turbulence levels (Durbin et al. 2000). To test hypotheses regarding plankton behavior response to turbulent motions, a laboratory apparatus is needed to simulate small-scale oceanic turbulence, which generally has an isotropic microstructure (e.g., Jiménez 1997; Yamazaki et al. 2002).

The research community has been interested in generating isotropic turbulence in the laboratory for many years, and a number of approaches have been employed. The most common technique for simulating near-isotropic small-scale turbulence in the laboratory has been the oscillating grid (e.g., Thompson and Turner 1975; Hopfinger and Toly 1976; McDougall 1979; Dickey et al. 1984; Brumley and Jirka 1987; Atkinson et al. 1987; De Silva and Fernando 1992, 1994; Cheng and Law 2001). The apparatus consists of an oscillating grid near one end of the tank that provides kinetic energy to the fluid and produces near-isotropic turbulence at distances sufficiently far from the grid (beyond three mesh sizes from the grid mid-plane, according to Cheng and Law 2001). Although this has been the preferred technique, grid-generated turbulence has several disadvantages. First, the induced flow field is not perfectly isotropic because, unavoidably, there is a unique direction in this flow (i.e., the direction perpendicular to the grid). Second, the flow is not homogeneous because the turbulence intensity decays away from the grid because of the inhomogeneous forcing. Hopfinger and Toly (1976) and others reported that the turbulent kinetic energy decays as a power law with distance from the grid. Third, the desire to control the turbulence intensity through adjustable stroke frequency and length often leads to fairly complicated lever mechanisms to drive the grid. The complexity generally increases the size and expense of the apparatus and limits its transportability.

Fourth, the grid itself or the lever mechanism often limits physical and optical access to the tank.

The oscillating-grid turbulence studies listed above addressed physical oceanography or fundamental fluid mechanics. Oscillating-grid apparatuses have also been used to address biological oceanography issues (e.g., Alldredge et al. 1990; Hill et al. 1992; Saiz and Alcaraz 1992; Saiz and Kiørboe 1995; MacKenzie and Kiørboe 1995; Landry et al. 1995). In this context, the oscillating grid apparatus has the additional disadvantage of placing an oscillating solid object near the creatures, which may be a hazard. Physical and optical access is also an important consideration for these studies because animals need to be taken in and out of the facility, and observations need to be made from several perspectives.

Alternative approaches for providing kinetic energy for the turbulent flow include mixing blades (e.g., Semenov 1965), electric fans (e.g., Birouk et al. 1996; Fallon and Rogers 2002), oscillating baffled cylinders (Chamorro 2001), two oscillating grids (Srdic et al. 1996), rotating cylindrical grids located in a strain field (Liu et al. 1999), and a towed grid (Dickey and Mellor 1980). These approaches often suffer from a lack of homogeneity (i.e., the statistical properties of the velocity fluctuations are a function of distance to the blades). Birouk et al. (1996), however, overcame this problem by placing one fan in each corner of a cubic chamber. The flow induced by the eight fans was nearly isotropic and homogeneous at the chamber center. Although data were not presented to support the assertion, Chamorro (2001) also claimed that the oscillating baffled cylinder produced homogeneous and isotropic turbulence. The towed grid approach was distinctly limited to a mode of operation with decaying turbulence in the wake of the grid. In any case, the fans, blades, baffles, or grids create a physical hazard for creatures in the flow.

Recently, Hwang and Eaton (2004) designed and constructed a unique apparatus to study solid particle movement in zero-gravity, gas-phase, isotropic turbulence. The apparatus consisted of a cubic box with actuators located at each corner. The actuators directed a synthetic jet through a small (1.9 cm) hole, an ejector tube, and a fixed mesh. Thus, a turbulent zero-net-mass-flux synthetic jet flow was directed from each corner toward the box center. The actuators were a superior driving mechanism for the particle-laden flow because particle contact with an oscillating grid would be an unquantifiable phenomenon during the experiments. The apparatus also needed to be portable to be placed on research aircraft simulating zero-gravity.

The purpose of this study is to test a new laboratory apparatus that has been designed to simulate approximately isotropic and homogeneous oceanic turbulence. Turbulence in the ocean occurs over a wide range of scales from large-scale global circulation (order of kilometers) to diffusive microscales (order of less than millimeters). At the scale of a zooplankton, i.e., the order of millimeters, the character of oceanic turbulence is generally isotropic, which means the turbulent fluctuations are, on average, independent of direction (e.g., Jiménez 1997; Yamazaki et al.
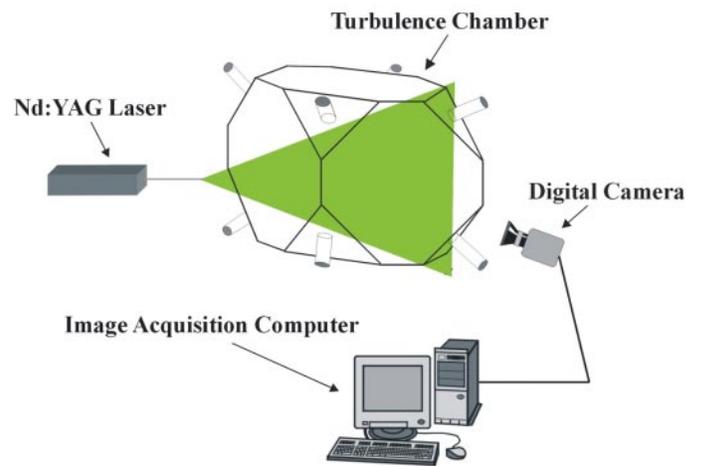
Fig. 1. Schematic of the experimental setup

2002). To produce turbulent motion with these characteristics, the Hwang and Eaton (2004) approach was adapted to a seawater environment. A set of operating parameters was established to produce turbulent fields with dissipation rates and microscales in the range for the coastal zone and wind-driven turbulent oceanic waters inhabited by plankton. The objective of this paper is to describe the apparatus and report the measured velocity and turbulence characteristics.

Materials and procedures

Description of the apparatus—The turbulence chamber consisted of a 0.4 m × 0.4 m × 0.4 m Plexiglas box with each corner replaced with an inclined surface to create a nearly spherical internal volume (Fig. 1). The size of the apparatus was large compared to zooplankton, but still relatively compact in the laboratory. Flow was generated in the chamber by synthetic jet actuators located at each of the eight corners (Fig. 2). The tank was filled with 30 ppt saltwater, and air bubbles were removed from the turbulence chamber and each actuator. The specified salinity level is consistent with regions of the ocean inhabited by zooplankton. All components of the apparatus were either plastic or 316 stainless steel to prevent corrosion in the saltwater environment. Optical access was equally available through all sidewalls (Fig. 2).

The net-zero-mass-flux actuators induced a synthetic jet toward the center of the turbulence chamber (Glezer and Amitay 2002). The actuator body was constructed with 5.08 cm PVC pipe (Fig. 2). A rubber (0.16-cm thick soft neoprene) diaphragm sandwiched between PVC flanges formed a movable endwall of the actuator chamber. The diaphragm was connected via a stainless steel rod to a woofer speaker (16.5 cm diameter cone) that was mounted at the end of the actuator. The oscillating motion of the diaphragm alternatively drew fluid into and forced fluid out of orifice holes in the turbulence chamber wall. Eight holes (0.32 cm diameter) were equally spaced around a 2.54 cm diameter circle centered on

Fig. 2. Photograph of the turbulence chamber and actuators

Table 1. Signal and DPIV measurement parameters

Turbulence Level	1	2	3	4
Signal Parameters				
Frequency (Hz)	40	35	30	30
Input Voltage (V)—Speaker 1	4.7	3.6	4.4	4.2
Input Voltage (V)—Speaker 2	6.5	4.0	5.8	7.0
Input Voltage (V)—Speaker 3	6.2	5.3	6.8	8.0
Input Voltage (V)—Speaker 4	5.6	3.8	5.2	5.2
Input Voltage (V)—Speaker 5	5.8	6.5	5.2	5.6
Input Voltage (V)—Speaker 6	6.7	6.5	4.8	5.0
Input Voltage (V)—Speaker 7	5.2	6.5	4.2	4.6
Input Voltage (V)—Speaker 8	6.9	5.7	3.8	4.2
DPIV Measurement Parameters				
Data Rate (Hz)	0.5	0.5	1.0	2.0
Nr of Velocity Fields	2000	2000	2000	2000
Measurement time (min)	67	67	33	17

the axis of each actuator. For the aqueous environment, this orifice arrangement was superior to a single large orifice hole (e.g., 1.9 cm diameter orifice used by Hwang and Eaton [2004]) because a synthetic jet formed at each hole for smaller diaphragm displacement (Smith and Glezer 1998). The resulting eight synthetic jets interacted to produce a broad jet-like flow originating from each corner of the turbulence chamber.

The synthetic jet strength (and hence the level of turbulence intensity in the chamber) was controlled by adjusting the frequency and amplitude of the signal driving the speakers. A low-power sinusoidal voltage signal was generated with a National Instruments DAQCard installed in a laptop computer. The signal was divided and amplified via an eight-channel power amplifier (individual digital control for each channel). The actuators were paired to have 180° phase difference (i.e., one actuator drew in fluid while its pair expelled fluid) to avoid fluid compressibility issues in the closed container.

Sinusoidal signals with frequencies ranging from 30 Hz to 40 Hz were used to drive the actuators at very small amplitudes (on the order of a millimeter or less). The input voltage for each speaker was adjusted to generate a near-zero mean flow in the center of the turbulence chamber, which was verified with the velocity measurements. Table 1 shows the frequency and voltage level for each speaker for each intensity level.

Velocity measurements—"Homogeneous turbulence" is defined as statistically invariant to shifts of the coordinate system, and "isotropic turbulence" is additionally invariant to rotations and reflections (Pope 2000). To test the flow in the apparatus for these conditions, we measured the velocity statistics. The test for near isotropy consisted of verifying that the magnitudes of the three Reynolds normal stresses were similar (i.e., $\overline{u_1'u_1'} \approx \overline{u_2'u_2'} \approx \overline{u_3'u_3'}$, or equivalently $u_{1rms} \approx u_{2rms} \approx u_{3rms}$) and that the Reynolds shear stresses and mean velocity were near zero ($\overline{u_1'u_2'} \approx \overline{u_1'u_3'} \approx \overline{u_2'u_3'} \approx 0$ and $U_1 \approx U_2 \approx U_3 \approx 0$). Note that whereas the apparent stress in the Reynolds-averaged Navier-Stokes equations is $-\rho\overline{u_i'u_j'}$, we have used the normal convention of also referring to $\overline{u_i'u_j'}$ as the Reynolds stress (e.g., Pope 2000). The test for near homogeneity consisted of verifying that the spatial variation of the velocity statistics was small.

A coordinate system was defined with the origin at the box center. The x_1 and x_2 coordinates correspond to the horizontal directions, and the x_3 coordinate corresponds to the vertical direction. Velocity measurements were performed during different time intervals in two perpendicular planes, namely the x_1-x_3 and x_2-x_3 planes.

Quantitative measurements of the flow and turbulence characteristics were obtained using Digital Particle Image Velocimetry (DPIV). This is a nonintrusive optical technique that measures fluid velocity by tracking the displacement of tracer particles. The measurement equipment and procedures have been previously described (Webster et al. 2001). The evaluation of the DPIV images consisted of correlation-based processing techniques to determine the displacement between two consecutive patterns of tracer particles (e.g., Raffel et al. 1998; software developed by Cowen and Monismith 1997). The particle displacement was combined with the image magnification and time delay between the laser pulses to determine the local velocity. Data were collected over sufficient time intervals to ensure statistical convergence (Table 1). In addition, the measurements demonstrated a high degree of repeatability.

Statistical measures of the turbulent field, such as the time average velocity and Reynolds stresses, were calculated from the velocity data. Because the velocity field was nearly isotropic

Table 2. Summary of statistics for each turbulence level, spatially averaged for the x_1-x_3 plane

Turbulence Level	1	2	3	4
$\langle U_1 \rangle$ (cm s^{-1})	–0.07	–0.03	0.18	0.07
$\langle U_3 \rangle$ (cm s^{-1})	–0.11	0.07	0.12	0.22
$\langle u_{1rms} \rangle$ (cm s^{-1})	0.081	0.30	0.69	0.88
$\langle u_{3rms} \rangle$ (cm s^{-1})	0.089	0.27	0.78	0.91
$\langle u_{1rms}/u_{3rms} \rangle$	0.91	1.11	0.89	0.98
$\langle \overline{u_1' u_3'} \rangle$ (cm^2 s^{-2})	0.001	–0.004	-0.002	–0.058
Skewness, u_1	–0.6	–0.5	0.0	0.1
Skewness, u_3	–0.2	0.2	0.1	–0.2
Kurtosis, u_1	3.5	3.3	3.2	3.2
Kurtosis, u_3	3.3	3.3	2.9	2.9

Table 3. Summary of statistics for each turbulence level, spatially averaged for the x_2-x_3 plane.

Turbulence Level	1	2	3	4
$\langle U_2 \rangle$ (cm s^{-1})	0.10	0.04	–0.12	0.07
$\langle U_3 \rangle$ (cm s^{-1})	–0.13	0.08	0.28	–0.10
$\langle u_{2rms} \rangle$ (cm s^{-1})	0.13	0.25	0.76	0.97
$\langle u_{3rms} \rangle$ (cm s^{-1})	0.15	0.29	0.76	0.96
$\langle u_{2rms}/u_{3rms} \rangle$	0.83	0.85	1.00	1.02
$\langle \overline{u_2' u_3'} \rangle$ (cm^2 s^{-2})	–0.006	–0.014	0.19	0.39
Skewness, u_2	0.5	0.1	0.0	–0.4
Skewness, u_3	-0.3	0.4	0.1	–0.2
Kurtosis, u_2	3.2	3.1	3.1	3.3
Kurtosis, u_3	2.6	3.2	2.8	3.0

and homogeneous, the surrogate expression is valid for the dissipation rate:

$$\varepsilon = 15\nu \overline{\left(\frac{\partial u_1'}{\partial x_1} \right)^2}. \tag{1}$$

This equation is the result of the symmetric properties of the fluctuating strain rate tensor for isotropic turbulence, where the full definition of the dissipation rate is $\varepsilon = 2\nu \overline{e_{ij}' e_{ij}'}$, and e_{ij}' is the strain rate tensor of the fluctuating velocity field (Pope 2000). The spatial gradient in Eq. 1 was estimated by a central finite difference approximation of the instantaneous vector field (a similar method was employed by Saarenrinne and Piirto [2000]). Saarenrinne and Piirto (2000) report that the best estimate of the dissipation rate with this method requires spatial resolution close to the Kolmogorov microscale. The current measurements have a spatial resolution finer than the Kolmogorov microscale for the lower two turbulence intensity levels and very near the Kolmogorov microscale for the higher two levels.

Based on the dissipation rate and other flow parameters, the Kolmogorov microscale $\eta \sim (\nu^3/\varepsilon)^{1/4}$, Taylor microscale $\lambda = \left(15\nu \overline{u_1'^2} / \varepsilon \right)^{1/2}$, and Taylor-scale Reynolds number $Re_\lambda = u_{1rms}\lambda/\nu$ were also calculated (Pope 2000).

Assessment

The velocity at a point in a turbulent flow appears "random" or "chaotic." Whereas the exact instantaneous velocity is impossible to predict, the overall behavior can be described stochastically and possesses certain universal characteristics. For instance, motions in a turbulent flow exist over a broad range of length (and time) scales, which correspond to fluctuating eddy motions. The largest (integral) scale is bounded by the geometric dimensions of the flow, for instance the diameter of a pipe or the depth of an ocean layer. The smallest length scale corresponds to eddies that dissipate kinetic energy into heat and is called the Kolmogorov microscale. The largest eddies draw energy from the mean flow motion, and

then transfer energy to successively smaller scales until it is dissipated at the Kolmogorov microscale. This process is referred to as the energy cascade. The energy distribution at the largest length scales is generally dictated by the flow geometry and mean flow speed. In contrast, the smallest length scales are many orders of magnitude smaller than the boundary constraints and hence are nearly isotropic in nature.

We expect that increasing the motion intensity will lead to an increase in Reynolds number, turbulent kinetic energy, and dissipation rate. The Kolmogorov microscale decreases for increasing dissipation rate, thus a broader range of eddy sizes exists for increased turbulence intensity (i.e., the largest length scale remains the same while the smallest length scale decreases). Thus, for higher Reynolds number, more intense, more rapidly evolving eddies over a broader range of scales are observed, but only on an average basis. At a particular instant and location, the fluid motion could correspond to anything within the range of scales described above. The data presented in this section confirm this general description of turbulence.

Velocity measurements were obtained for four turbulent intensity levels in the range of natural zooplankton habitats in coastal and wind-driven turbulence zones. The objective of this section is to quantify the nearly isotropic and homogeneous small-scale flow characteristics for each turbulence level. Field plots of statistical flow parameters facilitate a discussion of the magnitude and homogeneity of the turbulent characteristics. Also, the flow statistics were averaged over the center region (i.e., the 4 cm × 4 cm region at the center of the apparatus) to yield a single characteristic value for each statistical quantity (summarized in Tables 2 and 3, where $\langle \rangle$ indicates spatially averaged). Table 4 summarizes the turbulence parameters calculated from the measured flow fields.

Animations of the flow field for each turbulence intensity level are provided in Appendix 1. By observing the flow at any single location, it is apparent that the velocity fluctuates unpredictably, as expected in a turbulent flow. In addition, the sequence of instantaneous velocity fields presented in the ani-

Table 4. Summary of turbulence parameters for each level. Parameter values are the average of data for the x_1-x_3 and x_2-x_3 planes
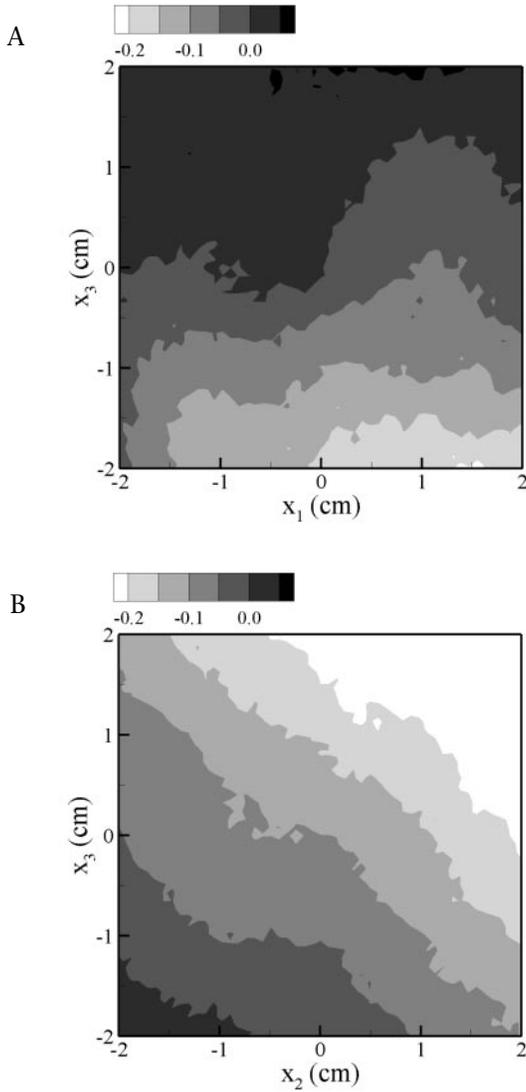
Turbulence Level	1	2	3	4
$\langle\varepsilon\rangle$ (cm^2 s^{-3})	0.002	0.009	0.096	0.25
η (cm)	0.15	0.10	0.057	0.045
λ (cm)	0.93	1.15	0.90	0.73
Re_λ	10	32	65	68

mations reveal the evolving spatial structure. To help visualize the evolving turbulent structure, the color of the vectors indicates the magnitude of vorticity. For each level, the flow consisted of intermittent ridges and valleys of vorticity that mark transition regions in the velocity field (i.e., gradients between relatively fast and slow fluid patches). Intermittent turbulent eddies are also apparent in the animations (indicated by vortex cores). Comparison among the cases is particularly illuminating; note that the right frame in each animation has the same reference vector and color scheme for ease of comparison. For turbulence level 1, the mild spatial variation of the velocity field and low levels of vorticity evolved very slowly. The velocity magnitude was also small compared to the other cases. Note that the Taylor-scale Reynolds number for this case was below the minimum required for "true" turbulence (i.e., $Re_\lambda \approx 30$; Jiménez 1997). Increasing the forcing led to several changes. For instance, the magnitude of the velocity and vorticity increased for each level. In addition, the spatial variation possessed finer structure (i.e., the higher ridges and lower valleys of vorticity are smaller and closer together), and the fields evolved more rapidly. Each of these characteristics contributed to the increasing turbulence intensity among the cases, which is quantified by the statistics reported in Tables 2 and 3.

The characteristics of turbulence level 2 are discussed in detail and compared with the other levels. The root mean square (rms) of the three velocity components (i.e., the square root of the Reynolds normal stresses) normalized by the spatially averaged value are shown in Fig. 3. The magnitude of the rms was similar for each component (Tables 2 and 3) and varied mildly over the measurement plane (roughly ± 20%, shown in Fig. 3). The spatial variation was similar for the other turbulence levels and the average values are reported in Tables 2 and 3. The spatially averaged ratios of the rms components were 1.11 and 0.85 for turbulence level 2 (Tables 2 and 3), which is close to the isotropic value of 1.0. The ratios of the rms components were similarly close to 1.0 for the other turbulence levels. Thus, the results indicate that the velocity fluctuations had a high degree of homogeneity and isotropy. For each turbulence level, the skewness of the velocity fluctuations was near zero and the kurtosis value was around three (Tables 2 and 3), which indicates that the velocity fluctuations have a near Gaussian distribution, as expected.

Fig. 4 shows mild spatial variation of the Reynolds shear stresses. The shear stresses are normalized by the turbulent
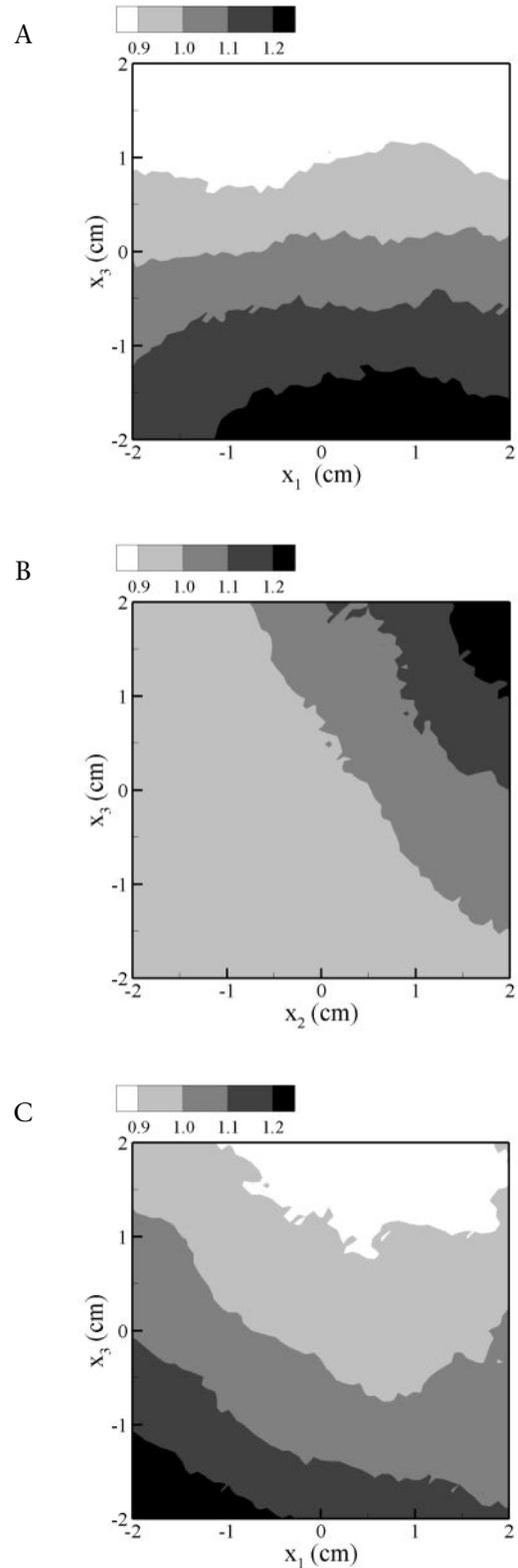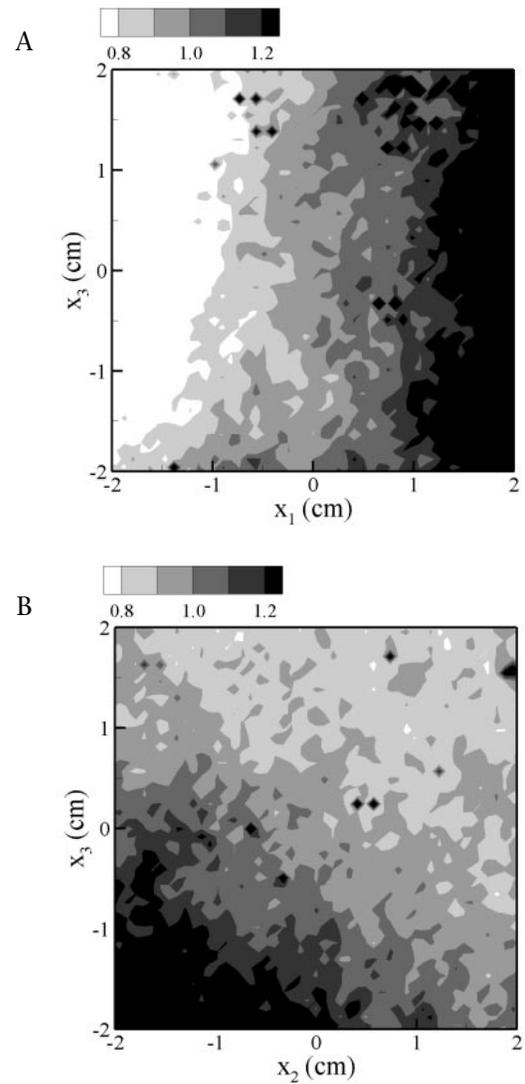

Fig. 3. Contour plots of the root mean square of the velocity fluctuations normalized by the spatially averaged value: (A) $u_{1rms}/\langle u_{1rms}\rangle$, (B) $u_{2rms}/\langle u_{2rms}\rangle$, and (C) $u_{3rms}/\langle u_{3rms}\rangle$, for turbulence level 2. The measurement plane is indicated by the axes.

Fig. 4. Contour plots of the Reynolds shear stresses normalized by the turbulent kinetic energy: (A) $\overline{u_1' u_3'} / \langle k \rangle$ and (B) $\overline{u_2' u_3'} / \langle k \rangle$ for turbulence level 2, where $\langle k \rangle = \frac{1}{2} \langle \overline{u_i u_i} \rangle$.

Fig. 5. Contour plots of the normalized dissipation rate, $\varepsilon / \langle \varepsilon \rangle$, for the (A) x_1-x_3 plane and (B) x_2-x_3 plane for turbulence level 2.

kinetic energy (spatially averaged value) to show that the shear stress was relatively small compared to the fluctuation intensity (contour levels indicate that the shear stresses are one order of magnitude smaller than the turbulent kinetic energy level). The data in Tables 2 and 3 also indicate that the mean velocity components were small compared to the rms of the velocity fluctuations. Similarly, relatively small values for the Reynolds shear stresses and mean velocity compared with the rms components were observed for the other turbulence levels. Thus, the criterion for isotropic flow that the mean velocity and Reynolds shear stresses be approximately zero was met reasonably well.

The dissipation rate, shown in Fig. 5, also did not deviate significantly from the spatially averaged value (roughly ± 20%)

and hence had a relatively high degree of homogeneity. The plots of dissipation rate for the other levels also were reasonably homogeneous (Fig. 6, again roughly ± 20%). In each case the spatial variation within each field was small compared to the jump in dissipation rate between cases.

The representative time record of the instantaneous dissipation rate illustrates the intermittency of the flow (Fig. 7) and qualitatively agrees with the time records of dissipation rate presented by Yeung (2001) for direct numerical simulation data. In fact, the peak value shown in this representative time record agrees almost exactly with the peak level shown by Yeung (2001). The intermittent high levels of dissipation rate correspond to strong, infrequent coherent vortices (Jiménez 1997). This further illustrates that a time-averaged quantity, such as the dissipation rate, masks the intermittent fluctua-

A

B

C
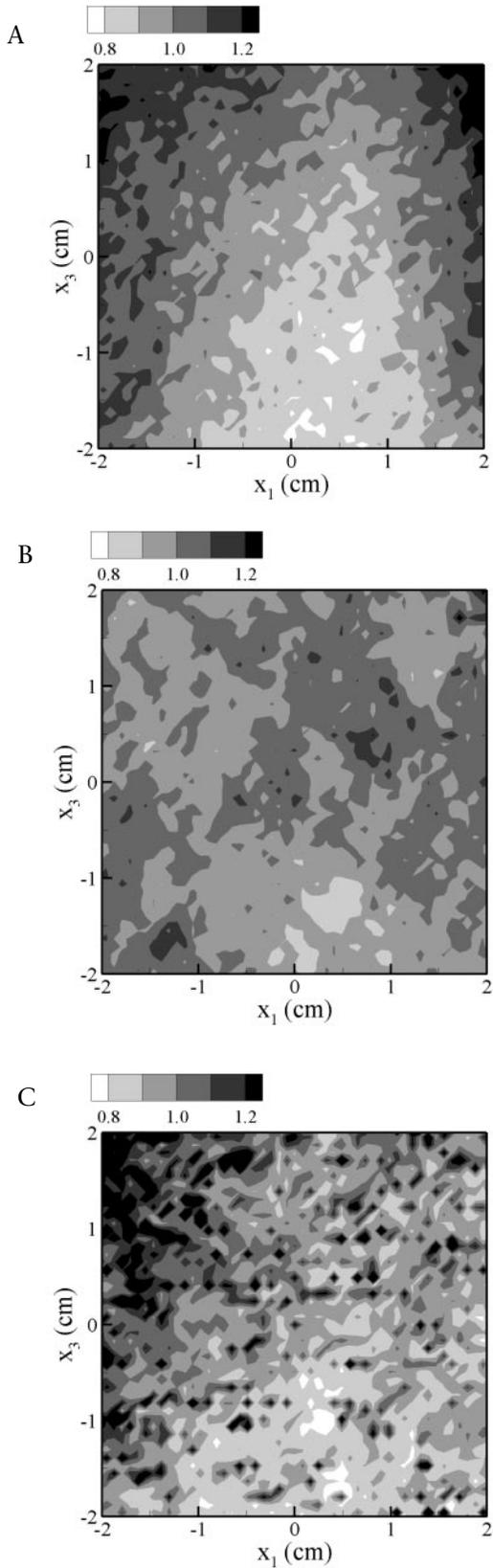
Fig. 6. Contour plots of the normalized dissipation rate, $\varepsilon/\langle\varepsilon\rangle$, for turbulence level (A) 1, (B) 3, and (C) 4.
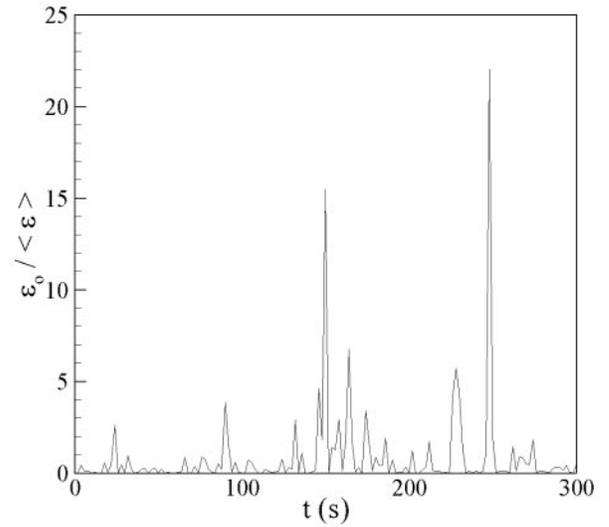
Fig. 7. Representative time record of the instantaneous dissipation rate, ε_0, normalized by the spatially averaged value for turbulence level 2.

tions of turbulent flows. For the dissipation rate, the instantaneous values may be an order of magnitude or larger than the time-averaged value. The intermittency underscores the need to collect very long time records of the flow field to capture a sufficient number of rare events for the statistical calculations (*see* Table 1 for the total length of the time record collected for each turbulence level).

Table 4 shows that the Kolmogorov microscale decreased with increasing turbulence intensity, as expected. The integral length scale is around 3 cm for each case; the precise value cannot be determined because the image acquisition field is too small to yield the complete spatial correlation function profile. The lack of variation among the cases reflected the fact that the integral length scale depends on the large scale geometry of the apparatus, which was constant among these cases. The Taylor-scale Reynolds number was small and varied from roughly 10 to 70 among the cases.

Discussion

The apparatus produced turbulent flow fields that are nearly isotropic and homogeneous. The flow fields did not perfectly agree with the theoretical ideal conditions, but they did possess many of the desired characteristics and compared favorably with grid-generated and alternative approaches. Contour plots of the dissipation rate showed a high degree of homogeneity with similar values in the two orthogonal measurement planes. For the oscillating grid apparatus, near homogeneous flow was achieved only in planes parallel to the grid at distances beyond a few mesh sizes from the grid mid-stroke plane. In addition, the ratios of the rms components were near unity for each case and for each measurement plane (range of 0.83 to 1.11 in Tables 2 and 3). This characteristic also compared well to pre-

vious designs. For instance, Hopfinger and Toly (1976) reported u_{3rms}/u_{1rms} in the range 1.1 to 1.3; De Silva and Fernando (1994) reported 1.1 to 1.2; Birouk et al. (1996) reported 0.9 to 1.1; and Hwang and Eaton (2004) reported 0.9 to 1.2.

As a practical note, the synthetic jet actuators were difficult to exactly balance for zero mean velocity at the center of the apparatus. This was evident from the fact that the mean velocity and Reynolds shear stresses were a fairly significant fraction of the turbulent kinetic energy for some of the cases. To exactly balance the flow, each of the eight synthetic jets needed to have the same momentum and correct orientation at the center of the box. Because inevitable construction and speaker response variations made each actuator unique, the jet strength was impossible to predict from the input voltage alone. Achieving "balanced" conditions at the center of the apparatus required a significant amount of trial and error. After this initial "calibration" process, the parameters in Table 1 produced repeatable flow conditions.

The problem of a finite mean velocity is not unique for the current apparatus. The oscillating grid apparatus also generated a substantial recirculating mean flow in the turbulence chamber (Thompson and Turner 1975; Brumley and Jirka 1987; Dohan and Sutherland 2002). Semenov (1965) and Fallon and Rogers (2002) also reported substantial mean velocity in their gas-phase apparatuses. The smallest relative mean velocity was reported for the gas-phase apparatus of Birouk et al. (1996) for a large Reynolds number flow.

Our primary objective was to build and test a new apparatus for studying individual zooplankton response to turbulent velocity fluctuations. Thus, we must address whether the turbulence characteristics and velocity and length scales are appropriate for these studies. Granata and Dickey (1991) and Kiørboe and Saiz (1995) report dissipation rates in the range of 10^{-3} to 1 cm²s⁻³ in the coastal zone, whereas the range of dissipation rate is lower for the open ocean (i.e., 10^{-6} to 10^{-2} cm²s⁻³). Hence, the range of dissipation rate produced in the new apparatus (Table 4) was consistent with the turbulence intensity levels in the coastal zone and for wind-driven turbulence (Jiménez 1997). The lowest dissipation rate created by the active operation of the actuators was 2×10^{-3} cm²s⁻³. When actuators are inactive, the water is nominally stagnant. Thus, zooplankton behavior additionally can be observed under flow conditions that mimic the very mild turbulence intensity observed in the deep pelagic.

Creating and quantifying turbulent fields with a dissipation rate less than 10^{-3} cm²s⁻³ is very difficult because the velocity magnitude is extremely small and the turbulent events are highly intermittent, which requires long sampling periods. The minimum dissipation rates produced by other laboratory studies focused on biological oceanography include Alldredge et al. (1990), 3×10^{-3} cm²s⁻³; Marrasé et al. (1990), 5×10^{-2} cm²s⁻³; Hill et al. (1992), 2.8×10^{-2} cm²s⁻³; Saiz and Alcaraz (1992), 1×10^{-2} cm²s⁻³; MacKenzie and Kiørboe (1995), 8×10^{-4} cm²s⁻³; and Saiz and Kiørboe (1995), 4×10^{-3} cm²s⁻³. In these studies, the dissipation rate was estimated through indirect

methods, and the details of the velocity fields were not reported. Thus, in contrast to the DPIV measurements reported herein, the turbulent characteristics, e.g., isotopic and homogeneous, of these flows are impossible to assess.

For the current flow conditions, the measured Kolmogorov microscale range also agreed with the range observed for the coastal zone and wind-driven turbulence (η in the range 0.04 to 0.2 cm; Kiørboe and Saiz 1995 and Jiménez 1997). Further, the values of the integral length scale (roughly 3 cm) and Kolmogorov microscale (Table 4) spanned the typical body size of zooplankton, which range roughly between 0.1 cm and 1 cm (Yamazaki and Squires 1996). The rms values of the velocity fluctuations (Tables 2 and 3) were also comparable to the nominal swimming speeds of zooplankton, which range between 0.1 cm/s and 1 cm/s (Yamazaki and Squires 1996) with escape speeds of 100 cm/s (Yen 1988).

In the past several years, a handful of investigators have addressed zooplankton behavior response to flow. In these studies, the animal was subjected to a simple flow pattern (e.g., siphon flow by Fields and Yen 1996, 1997; Titelman 2001; Titelman and Kiørboe 2003; and siphon, oscillating chamber, Couette, and solid body rotation flows by Kiørboe et al. 1999). Behavior response to several flow parameters, such as acceleration, vorticity, and strain rate, were considered. Fields and Yen (1996) observed that shear strain rate was the least variable parameter that elicited a response. Kiørboe et al. (1999) similarly concluded that strain rate was the important flow parameter and that the threshold level was independent of linear versus shear strain rate.

Because turbulence is a time-varying three-dimensional flow (*see* Appendix 1), it is important to review the formal description of flow fields in the context of zooplankton mechanoreception. When describing a flow field, the velocity gradient can be decomposed into pure deformation and pure rotation components:

$$\overline{\nabla}\overline{u} = \frac{\partial u_i}{\partial x_j} = \begin{bmatrix} \frac{\partial u_1}{\partial x_1} & \frac{\partial u_2}{\partial x_1} & \frac{\partial u_3}{\partial x_1} \\ \frac{\partial u_1}{\partial x_2} & \frac{\partial u_2}{\partial x_2} & \frac{\partial u_3}{\partial x_2} \\ \frac{\partial u_1}{\partial x_3} & \frac{\partial u_2}{\partial x_3} & \frac{\partial u_3}{\partial x_3} \end{bmatrix} = \underbrace{\frac{1}{2}\left(\frac{\partial u_i}{\partial x_j} + \frac{\partial u_j}{\partial x_i}\right)}_{symmetric\ part} + \underbrace{\frac{1}{2}\left(\frac{\partial u_i}{\partial x_j} - \frac{\partial u_j}{\partial x_i}\right)}_{anti-symmetric\ part}$$

where we have employed the standard index notation in which *i* and *j* are each implied to be 1, 2, and 3 in a three-dimensional coordinate system. The antisymmetric component is called the rotation tensor and the elements correspond to the vorticity vector (i.e., $\overline{\omega} = \overline{\nabla} \times \overline{u}$ or $\omega_k = \frac{\partial u_i}{\partial x_j} - \frac{\partial u_j}{\partial x_i}$). The instantaneous values of the vorticity are shown in Appendix 1. The symmetric part of the velocity gradient tensor is called the strain rate tensor (or equivalently the rate of deformation tensor):

$$e_{ij} = \frac{1}{2}\left(\frac{\partial u_i}{\partial x_j} + \frac{\partial u_j}{\partial x_i}\right) = \begin{bmatrix} \frac{\partial u_1}{\partial x_1} & \frac{1}{2}\left(\frac{\partial u_2}{\partial x_1} + \frac{\partial u_1}{\partial x_2}\right) & \frac{1}{2}\left(\frac{\partial u_3}{\partial x_1} + \frac{\partial u_1}{\partial x_3}\right) \\ \frac{1}{2}\left(\frac{\partial u_2}{\partial x_1} + \frac{\partial u_1}{\partial x_2}\right) & \frac{\partial u_2}{\partial x_2} & \frac{1}{2}\left(\frac{\partial u_3}{\partial x_2} + \frac{\partial u_2}{\partial x_3}\right) \\ \frac{1}{2}\left(\frac{\partial u_3}{\partial x_1} + \frac{\partial u_1}{\partial x_3}\right) & \frac{1}{2}\left(\frac{\partial u_3}{\partial x_2} + \frac{\partial u_2}{\partial x_3}\right) & \frac{\partial u_3}{\partial x_3} \end{bmatrix}.$$
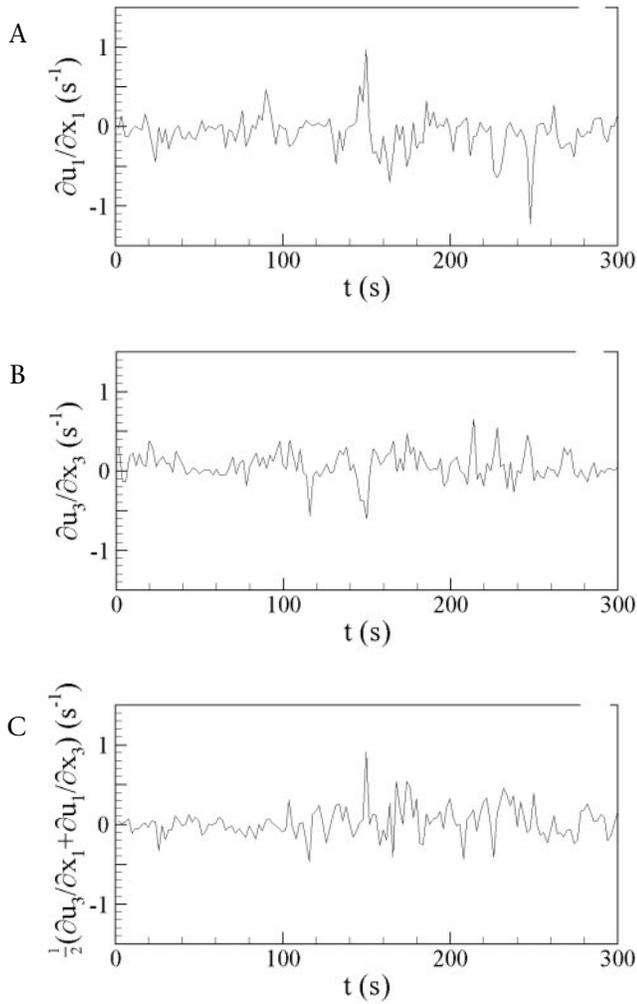
Fig. 8. Representative time records of the instantaneous strain rates, (A) $\frac{\partial u_1}{\partial x_1}$, (B) $\frac{\partial u_3}{\partial x_3}$, and (C) $\frac{1}{2}\left(\frac{\partial u_3}{\partial x_1}+\frac{\partial u_1}{\partial x_3}\right)$ for turbulence level 2.

The components of the strain rate tensor correspond to the physical deformation of the local fluid element, which occurs in two fundamental modes. The elements on the diagonal of the tensor (e.g., $\partial u_1/\partial x_1$) correspond to extension or contraction along the respective coordinate directions and are called "linear" strain rates. The off-diagonal components correspond to an angular squeezing or expansion and are called "shear" strain rates. There are three linear strain rates and three independent shear strain rates.

In turbulent flows, the strain rate field fluctuates randomly in a manner similar to the velocity and vorticity fields shown in Appendix 1. For the nearly homogeneous flow fields presented herein, the mean strain rate was close to zero because the mean velocity gradients were very small. In addition, zooplankton are likely to respond to the instantaneous flow field instead of a time-averaged value (e.g., Fields et al. 2002). Fig. 8 shows representative time records for three strain rate components at an arbitrary location in the flow. The time records

Table 5. Summary of the standard deviation of the instantaneous strain rates for each turbulence level

Turbulence Level	1	2	3	4
$\left\langle\left(\frac{\partial u_1}{\partial x_1}\right)_{std\,dev}\right\rangle$ (s^{-1})	0.11	0.25	0.78	1.06
$\left\langle\left(\frac{\partial u_2}{\partial x_2}\right)_{std\,dev}\right\rangle$ (s^{-1})	0.11	0.22	0.80	1.26
$\left\langle\left(\frac{\partial u_3}{\partial x_3}\right)_{std\,dev}\right\rangle$ (s^{-1})	0.12	0.25	0.79	1.13
$\left\langle\frac{1}{2}\left(\frac{\partial u_3}{\partial x_1}+\frac{\partial u_1}{\partial x_3}\right)_{std\,dev}\right\rangle$ (s^{-1})	0.081	0.20	0.64	0.86
$\left\langle\frac{1}{2}\left(\frac{\partial u_3}{\partial x_2}+\frac{\partial u_2}{\partial x_3}\right)_{std\,dev}\right\rangle$ (s^{-1})	0.092	0.19	0.66	0.99

suggest that each instantaneous strain rate component at this point in space could be any value within a fairly wide range. Thus, an appropriate statistical measure of the fluctuating strain rate is the standard deviation:

$$\left(\frac{\partial u_1}{\partial x_1}\right)_{std\,dev} = \left\{\frac{1}{N-1}\sum_{n=1}^{N}\left(\left(\frac{\partial u_1}{\partial x_1}\right)_n - \overline{\frac{\partial u_1}{\partial x_1}}\right)^2\right\}^{1/2}, \text{ for example.}$$

The standard deviation of five components of the strain rate tensor (three linear strain rates and two shear strain rates) is shown in Table 5 for each turbulence level. The data have been averaged over the center 4 cm × 4 cm region of the apparatus as indicated by the $\langle\ \rangle$ notation. For each turbulence level, the standard deviation of the three linear strain rates have similar values, which again confirms the nearly isotropic nature of the flow fields. In the context of zooplankton mechanoreception, the standard deviation provides a metric of the magnitude of the fluctuating strain rate, but it is important to remember that the instantaneous fluctuations occur at random intervals and could be significantly larger, as shown in Fig. 8.

While there appears to be some agreement that the important mechanosensory cue is strain rate, the threshold values that elicit response appear highly variable among species and researchers. For instance, Fields and Yen (1997) report that 50% of *Acartia tonsa* adults respond with an escape for a shear strain rate of 0.75 s^{-1}. Kiørboe et al. (1999) report that *Acartia tonsa* respond at a threshold strain rate of 0.4 s^{-1} independent of linear versus shear strain rate. Fields and Yen (1997) further reported that the escape response was highly dependent on the species and on the stage of development. The threshold of shear strain rate for which 50% of the specimens responded varied between 0.75 s^{-1} and 26 s^{-1} depending on species. Titelman (2001) and Titelman and Kiørboe (2003) report critical strain rate values in the range of 0.5 to 4.3 s^{-1} for nauplii and copepodids depending on the species and stage. Viitasalo et al. (1998) similarly observed that copepods possess important differences in escape capabilities among species.

Whereas these studies provide some guidance regarding the threshold strain rates that elicit response, it is important to distinguish that they address the behavior response to *mean* strain rates. The response to a fluctuating strain rate field may be, and

seems likely to be, very different. The data in Table 5 show that the standard deviation of the fluctuating strain rate varied by roughly an order of magnitude among the turbulence levels (i.e., 0.1 to 1 s^{-1}). As discussed above, the reported magnitude of the mean strain rate that elicits response of adult *Acartia tonsa* is roughly in the middle of the range (Fields and Yen 1997 and Kiørboe et al. 1999). However, the applicability of these mean strain rate thresholds to turbulent flows is unknown.

This study achieved the primary objective of building and testing a new apparatus that is appropriate for studying zooplankton response to turbulent velocity fluctuations. The flow characteristics in the center of the apparatus have been confirmed to be reasonably isotropic and homogeneous. The dissipation rate and Kolmogorov microscale agreed well with coastal zone and wind-driven turbulent environments, and the length scales and magnitude of the velocity fluctuations were appropriate for zooplankton response studies. In addition, the range of fluctuating strain rate agreed with the observed behavior response of several copepods species with the caveat that the response to a fluctuating turbulent flow may be different than the response to a contrived laminar flow such as a steady siphon. The flow fields in the new apparatus also possessed the intermittent characteristics expected in turbulent oceanic flows. The apparatus is additionally superior to grid oscillating designs because of increased simplicity, increased controllability, increased transportability, and reduced cost. The net-zero-mass-flux actuators are also ideal for biological oceanographic research because no moving objects are located inside the test section.

The apparatus now provides a valuable tool for biological oceanographic research. In particular, the next phase of research will involve the study of zooplankton behavior patterns for the four turbulence levels that have been parameterized, plus the stagnant case. The turbulent characteristics can be matched to natural habitats or varied to document the rate of change in zooplankton behavior. Our capability to visualize both the instantaneous velocity field (e.g., Webster et al. 2001) and instantaneous plankton behavior (e.g., Yen and Fields 1992; Fields and Yen 1997; Doall et al. 1998) enables studies of directional responses to coherent small-scale turbulent structures. The instantaneous strain rate, vorticity, and acceleration will be calculated from the measured velocity fields and then correlated with observed behavior. Preliminary observations reveal that zooplankton pass through the measurement region for all turbulence levels discussed here. The frequency of these events depends on the number of animals in the chamber, the species, and other factors.

Furthermore, because the apparatus is compact (see the photograph in Fig. 2) and is controlled from a laptop computer, the apparatus can be brought onto a research ship. In that case, animal specimens would be collected from the ocean and moved to the apparatus on the ship. The apparatus is a closed container, thus sloshing of a free surface in the tank due to ship movement is not an issue. The apparatus' seaworthiness can be evaluated in future tests; we anticipate that it will perform well for shipboard operation during calm sea conditions. Observations of behavior response to controlled and well-quantified turbulence then could be performed immediately after specimen collection.

References

Alldredge, A. L., T. C. Granata, C. C. Gotschalk, and T. D. Dickey. 1990. The physical strength of marine snow and its implications for particle disaggregation in the ocean. Limnol. Oceanogr. 35:1415-1428.

Atkinson, J. F., L. Damiani, and D. R. F. Harleman. 1987. A comparison of velocity measurements using a laser anemometer and a hot-film probe, with application to grid-stirring entrainment experiments. Phys. Fluids 30:3290-3292.

Birouk, M., C. Chauveau, B. Sarh, A. Quilgars, and I. Gokalp. 1996. Turbulence effects on the vaporization of monocomponent single droplets. Combustion Sci. Tech. 113:413-428.

Brumley, B. H., and G. H. Jirka. 1987. Near-surface turbulence in a grid-stirred tank. J. Fluid Mech. 183:235-263.

Chamorro, V. C. 2001. The effects of small scale turbulence in the feeding ecology and swimming speed of fathead minnow larvae (*Pimephales promelas*), inland silverside larvae (*Menidia beryllina*) and the lobate ctenophore (*Mnemiopsis leidyi*). M.S. Thesis, University of Maryland.

Cheng, N. -S., and A. W. -K. Law. 2001. Measurements of turbulence generated by oscillating grid. J. Hydraulic Eng. 127:201-208.

Cowen, E. A., and S. G. Monismith. 1997. A hybrid digital particle tracking velocimetry technique. Exp. Fluids 22:199-211.

De Silva, I. P. D., and H. J. S. Fernando. 1992. Some aspects of mixing in a stratified turbulent patch. J. Fluid Mech. 240:601-625.

———, and H. J. S. Fernando. 1994. Oscillating grids as a source of nearly isotropic turbulence. Phys. Fluids 6:2455-2464.

Dickey, T. D., B. Hartman, D. Hammond, and E. Hurst. 1984. A laboratory technique for investigating the relationship between gas transfer and fluid turbulence. p. 93-100. *In* W. Brutsaert and G.H. Jirka [eds.], Gas transfer at water surfaces. D. Reidel.

———, and G. L. Mellor. 1980. Decaying turbulence in neutral and stratified fluids. J. Fluid Mech. 99:13-31.

Doall, M. H., S. P. Colin, J. R. Strickler, and J. Yen. 1998. Locating a mate in 3D: The case of *Temora longicornis*. Phil. Trans. Royal Society of London 353:681-689.

Dohan, K., and B. R. Sutherland. 2002. Turbulence time scales in mixing box experiments. Exp. Fluids 33:709-719.

Dower, J. F., T. J. Miller, and W. C. Leggett. 1997. The role of microscale turbulence in the feeding ecology of larval fish. Adv. Mar. Biology 31:169-220.

———, P. Pepin, and W. C. Leggett. 1998. Enhanced gut fullness and an apparent shift in size selectivity by radiated shanny (*Ulvaria subbifurcata*) larvae in response to increased turbulence. Can. J. Fish. Aquat. Sci. 55:128-142.

Durbin, E. G., P. R. Garrahan, and M. C. Casas. 2000. Abundance and distribution of *Calanus finmarchicus* on the Georges Bank during 1995 and 1996. ICES J. Mar. Sci. 57:1664-1685.

Fallon, T., and C. B. Rogers. 2002. Turbulence-induced preferential concentration of solid particles in microgravity conditions. Exp. Fluids 33:233-241.

Fields, D. M., D. S. Shaeffer, and M. J. Weissburg. 2002. Mechanical and neural responses from the mechanosensory hairs on the antennule of *Gaussia princeps*. Mar. Ecol. Prog. Ser. 227:173-186.

———, and J. Yen. 1996. The escape behavior of *Pleuromamma xiphias* in response to a quantifiable fluid mechanical disturbance. p. 323-340. *In* P.H. Lenz, D.K. Hartline, J.E. Purcell, and D.L. MacMillan [eds.], Zooplankton: sensory ecology and physiology, Vol. 1. Gordon and Breach.

———, and ———. 1997. The escape behavior of marine copepods in response to a quantifiable fluid mechanical disturbance. J. Plankton Res. 19:1289-1304.

Franks, P. J. S. 2001. Turbulence avoidance: An alternate explanation of turbulence-enhanced ingestion rates in the field. Limnol. Oceanogr. 46:959-963.

Glezer, A., and M. Amitay. 2002. Synthetic jets. Ann. Rev. Fluid Mech. 34:503-529.

Granata, T. C., and T. D. Dickey. 1991. The fluid-mechanics of copepod feeding in a turbulent flow: a theoretical approach. Prog. Oceanogr. 26:243-261.

Heath, M. R., E. W. Henderson, and D. L. Baird. 1988. Vertical distribution of herring lavae in relation to physical mixing and illumination. Mar. Ecol. Prog. Ser. 47:211-228.

Hill, P. S., A. R. M. Nowell, and P. A. Jumars. 1992. Encounter rate by turbulent shear of particles similar in diameter to the Kolmogorov scale. J. Marine Res. 50:643-668.

Hopfinger, E. J., and J. A. Toly. 1976. Spatially decaying turbulence and its relation to mixing across density interfaces. J. Fluid Mech. 78:155-175.

Hwang, W., and J. K. Eaton. 2004. Creating homogeneous and isotropic turbulence without a mean flow. Exp. Fluids. 36(2).

Incze, L. S., D. Hebert, N. Wolff, N. Oakey, and D. Dye. 2001. Changes in copepod distributions associated with increases turbulence from wind stress. Mar. Ecol. Prog. Ser. 213:229-240.

Jiménez, J. 1997. Oceanic turbulence at millimeter scales. Scientia Marina 61:47-56.

Kiørboe, T., and E. Saiz. 1995. Planktivorous feeding in calm and turbulent environments, with emphasis on copepods. Mar. Ecol. Prog. Ser. 122:135-145.

———, ———, and A. Visser. 1999. Hydrodynamic signal perception in the copepod *Acartia tonsa*. Mar. Ecol. Prog. Ser. 179:97-111.

Lagadeuc, Y., M. Boule, and J. J. Dodson. 1997. Effect of vertical mixing on the vertical distribution of copepods in coastal waters. J. Plankton Res. 19:1183-1204.

Landry, F., T. J. Miller, and W. C. Leggett. 1995. The effects of small-scale turbulence on the ingestion rate of fathead minnow (*Pimephales promelas*) larvae. Can. J. Fish. Aquat. Sci. 52:1714-1719.

Liu, S., J. Katz, and C. Meneveau. 1999. Evolution and modelling of subgrid scales during rapid straining of turbulence. J. Fluid Mech. 387:281-320.

Mackas, D. L., H. Sefton, C. B. Miller, and A. Raich. 1993. Vertical habitat partitioning by large calanoid copepods in the oceanic sub-arctic Pacific during spring. Prog. Oceanogr. 32:259-294.

Marrasé, C., J. H. Costello, T. Granata, and J. R. Strickler. 1990. Grazing in a turbulent environment: energy dissipation, encounter rates, and efficacy of feeding currents in *Centropages hamatus*. Proc. Nat. Acad. Sci. USA 87:1653-1657.

MacKenzie, B. R., and T. Kiørboe. 1995. Encounter rate and swimming behavior of pause travel and cruise larval fish predators in calm and turbulent environments. Limnol. Oceanogr. 40:1278-1289.

———, and ———. 2000. Larval fish feeding and turbulence: A case for the downside. Limnol. Oceanogr. 45:1-10.

McDougall, T. J. 1979. Measurements of turbulence in a zero-mean-shear mixed layer. J. Fluid Mech. 94:409-431.

Pope, S. B. 2000. Turbulent flows. Cambridge University Press.

Raffel, M., C. E. Willert, and J. Kompenhans. 1998. Particle image velocimetry: a practical guide. Springer-Verlag.

Rothschild, B. J., and T. R. Osborn. 1988. Small-scale turbulence and plankton contact rates. J. Plankton Res. 10:465-474.

Saarenrinne, P., and M. Piirto. 2000. Turbulent kinetic energy dissipation rate estimation from PIV velocity vector fields. Exp. Fluids 29 Suppl.: S300-S307.

Saiz, E., and M. Alcaraz. 1992. Free-swimming behavior of *Acartia clausi* (Copepoda: Calanoida). Under turbulent water movement. Mar. Ecol. Prog. Ser. 80:229-236.

———, and T. Kiørboe. 1995. Predatory and suspension feeding of the copepod *Acartia tonsa* in turbulent environments. Mar. Ecol. Prog. Ser. 122:147-158.

Semenov, E. S. 1965. Measurement of turbulence characteristics in a closed volume with artificial turbulence. Combust. Explos. Shock Waves 1:57-62.

Smith, B. L., and A. Glezer. 1998. The formation and evolution of synthetic jets. Phys. Fluids 10:2281-2297.

Srdic, A., H. J. S. Fernando, and L. Montenegro. 1996. Generation of nearly isotropic turbulence using two oscillating grids. Exp. Fluids 20:395-397.

Titelman, J. 2001. Swimming and escape behavior of copepod nauplii: implications for predator-prey interactions among copepods. Mar. Ecol. Prog. Ser. 213:203-213.

———, and T. Kiørboe. 2003. Predator avoidance by nauplii. Mar. Ecol. Prog. Ser. 247:137-149.

Thompson, S. M., and J. S. Turner. 1975. Mixing across an interface due to turbulence generated by an oscillating grid. J. Fluid Mech. 67:349-368.

Viitasalo, M., T. Kiorboe, J. Flinkman, L.W. Pedersen, and A.W.

Visser. 1998. Predation vulnerability of planktonic copepods: consequences of predator foraging strategies and prey sensory abilities. Mar. Ecol. Prog. Ser. 175:129-142.

Webster, D. R., P. J. W. Roberts, and L. Ra'ad. 2001. Simultaneous DPTV/PLIF measurements of a turbulent jet. Exp. Fluids 30:65-72.

Yamazaki, H., D. L. Mackas, and K. L. Denman. 2002. Coupling small-scale physical processes with biology. p. 51-112. *In* A. R. Robinson, J. J. McCarthy, and B. J. Rothschild [eds.], The Sea. Volume 12. Wiley.

———, and K. D. Squires. 1996. Comparison of oceanic turbulence and copepod swimming. Mar. Ecol. Prog. Ser. 144:299-301.

Yen, J. 1988. Directionality and swimming speeds in predator-prey and male-female interactions of *Euchaeta rimana*, a subtropical marine copepod. Bull. Mar. Sci. 43:395-403.

———, and D. M. Fields. 1992. Escape responses of *Acartia hudsonica* nauplii from the flow field of *Temora longicornis*. Archiv für Hydrobiologie Beiheft 36:123-134.

Yeung, P. K. 2001. Lagrangian characteristics of turbulence and scalar transport in direct numerical simulations. J. Fluid Mech. 427:241-274.